JOURNAL OF SPACECRAFT AND ROCKETS
Vol. 29, No. 4, July-August 1992

# Engineering Notes

*ENGINEERING NOTES are short manuscripts describing new developments or important results of a preliminary nature. These Notes cannot exceed 6 manuscript pages and 3 figures; a page of text may be substituted for a figure and vice versa. After informal review by the editors, they may be published within a few months of the date of receipt. Style requirements are the same as for regular contributions (see inside back cover).*

## CRRES Magnetic Electron Spectrometer AFGL-701-5A (MEA)

A. L. Vampola,* J. V. Osborn,† and B. M. Johnson†
*The Aerospace Corporation,*
*Los Angeles, California, 90009*

### Instrument Description

THE medium electrons A (MEA) instrument utilizes a design which had extensive use in low-energy nuclear research laboratories through the early years of the atomic age and is very well understood.[1] The measurement principle used is momentum analysis in a solenoidal magnetic field. In a 180 deg magnetic electron spectrometer, particles entering an aperture encounter a uniform solenoidal magnetic field and travel a circular path in the plane transverse to the field. After being bent through approximately 180 deg, the particle is detected by a planar array. First order focusing occurs in the plane. Electrons with the same energy, although at different angles, are focused on almost the same vertical line on the detection plane. There is no focusing in the vertical direction. The focusing in the plane occurs because the length of a chord subtending angles near 180 deg in a circle does not change rapidly with a change in the subtended angle (the chord is similar in length to the diameter, which is the 180 deg chord). Monoenergetic electrons entering through an aperture width $w$ will have an image width $w'$ given by

$$w' = w + 2\rho(1 - \cos\theta) \tag{1}$$

where $\rho$ is the radius of curvature and $\theta$ is the aperture half-angle. For the MEA, this amounts to less than 1% image broadening.

In a uniform magnetic field, the motion of a charged particle moving perpendicular to the field is given by

$$\boldsymbol{Bvq} = \boldsymbol{mv}^2/\rho \tag{2}$$

Equation (2) just equivalences the electric force on the charge $q$ due to motion across the magnetic field $\boldsymbol{B}$ with the centrifugal force on a particle of mass $\boldsymbol{m}$ and velocity $\boldsymbol{v}$ gyrating in a circle with radius $\rho$. Thus, in a magnetic electron spectrometer, the energy analysis is done by geometric means ($\boldsymbol{B}$ and $\rho$) and the information derived from the energy deposit in the detector can be used for other purposes. In the case of the MEA, this information is used to increase the efficiency of detection to approximately 100% and to identify penetrating particle backgrounds (energetic protons in the inner zone and cosmic rays).

Received June 9, 1991; revision received Aug. 6, 1991; accepted for publication Aug. 6, 1991. 

*Consultant; current address: P.O. Box 10225, Torrance, CA 90505. Associate Fellow AIAA.
†Member of Technical Staff, P.O. Box 92957.

Since the physics of the instrument is well understood, the geometric factors, the energy responses, and the efficiencies of the individual channels can be determined with very good accuracy through computational means. The approach is to calculate the energy and angle cutoffs for each channel and then to use electron beam tests to verify the proper operation of the instrument. The mathematical model is then used to calculate the detailed response of the instrument. In the usual case, the magnetic field in the chamber of a magnetic electron spectrometer is quite uniform. The two-dimensional angular response can be checked quite accurately and the energy cutoffs of each channel can be determined with a precision that is limited only by the energy spread of the particle beam used in the determination. As a result, data from magnetic electron spectrometers can be used for absolute calibrations.

Figure 1 shows a schematic outline of the MEA analyzing chamber. The chamber consists of two halves which were milled out of Armco magnetic iron (a low coercive-force oxygen-free material). The low coercive-force material provides a relatively low-weight yoke with a low fringing field. The permanent magnet utilized is made from Indox V, a ceramic material with high coercive force. A high coercive force is needed to ensure stability in the field intensity throughout launch vibration, temperature variations, rotation in the earth's magnetic field, etc. The Indox V is stabilized by disassembling the yoke after the Indox V has been magnetized in it. When reassembled, the field intensity returns along a minor hysteresis loop with a lower total field intensity, but much better stability, than it had previously. The external collimator consists of a series of thin tungsten aperture plates held in an aluminum assembly. The internal collimator is entirely tungsten. A disk-loaded collimator is an absolute necessity for an electron spectrometer because of the ease with which electrons backscatter out of material. The disk-loaded collimator acts as a true collimator, whereas a smooth wall would act as a funnel. The MEA also incorporates antiscatter structures within the chamber. The top and bottom of the chamber have aluminum face plates with milled vertical ridges. The sides of the chamber have aluminum fins extending out to the working

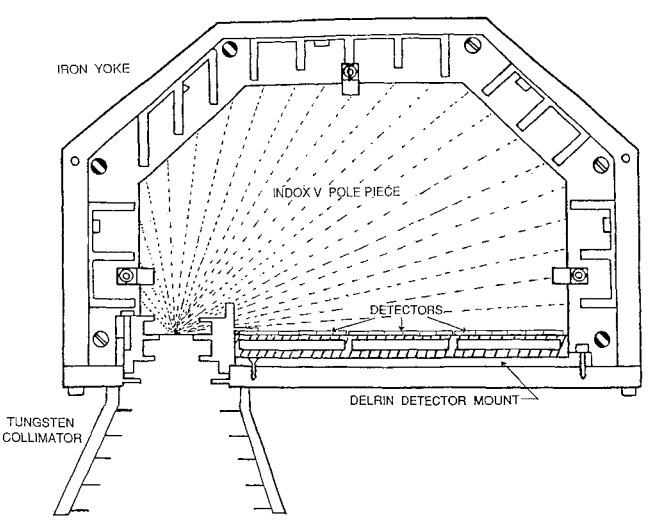


**Fig. 1. Layout diagram of the CRRES MEA.**

volume of the magnetic field. These ridges and fins ensure that an electron must undergo numerous scatterings in a low Z material in order to reach a detector unless its trajectory lies entirely within the collimator acceptance zone. The sole exception is a scattering from the top of one of the ridges or fins. The aluminum fins and face plates are anodized and coated with a black conductive paint to reduce light scattering to the detectors and to prevent charge buildup on the plates (which would cause unwanted, and uncontrolled, focusing in the vertical direction).

At the 180 deg focus, the electrons impinge upon a detector array consisting of six ion-implanted silicon plates mounted in three pairs on a thick circuit card. One of each pair is mounted on the front of the circuit card over a window through the card. The other member of each pair is mounted behind the window in registration with its partner. Each of the silicon plates is nominally 1.55 cm wide, 6.05 cm long, and 0.50 mm thick. The window is 1.45 × 5.95 cm. Each plate has six metallized areas nominally 0.95 × 1.45 cm with a 0.5-mm separation. Corresponding metallizations on the front and rear silicon plates are tied together electrically to form a single detector with a nominal thickness of 1 mm. Thus, there are a total of 18 detection areas in the linear array.

Circuitry for the MEA is typical of most charge-sensitive amplifier applications. Each detector channel consists of the detector and bias network; a preamplifier with a JFET input configured as a charge integrator; a pole-zero cancellation network; two stages of amplification and shaping; active baseline restoration followed by a pair of stacked discriminators; and a TTL logic level, 1-$\mu$s pulse generation circuit. The output pulses are sent to accumulators in a data processing unit[2] (DPU) and eventually telemetered with a 0.512-s resolution.

Generation of a particle count is initiated by an electron impinging on a detector configured as a reverse-biased P-N diode and depositing most of or all of its energy as charge pairs, at a rate of 3.6 eV/pair, in the depletion region of the N-type silicon. The charge pairs are swept out of the depletion region by the biasing network, creating a charge pulse which is proportional to the energy of the incident electron minus any energy lost as bremsstrahlung or residual electron energy (the electrons which may backscatter out of the detector). The charge is integrated on a 1-pf feedback capacitor, resulting in a sharply rising (5 ns), exponentially decaying ($T_{rc}$ = 10 $\mu$s) voltage pulse (44.4 mv/MeV deposited energy) at the output of the preamplifier. The feedback capacitors were selected to be within 0.1% of each other. The preamplifier JFETs (2N4858) were selected for maximal transconductance and minimal noise.

The preamplifier feeds a network that is tuned to cancel the pole in the transfer function of the preamplifier network with a zero. This pole-zero cancellation network removes the undershoot recovery of the output pulse and also ac couples the preamplifier to the amplification and shaping stages of the circuit. The shaping section smooths the preamplifier output pulse into a semi-Gaussian pulse ($t_s$ = 2 $\mu$s). At the last stage of amplification, there is an active baseline restore feedback loop to ensure that with rate changes or age the offsets of the system will always be compensated to a zero baseline. The overall analog noise measured with an equivalent detector capacitance was ~ 6 keV for all channels. The detector noise levels are much higher (15–20 keV at launch). Finally, two stacked discriminators bracketed the pulse height in energy from 50%–110% of the minimum and maximum energy electron focused upon the detector associated with that channel. The pole-zero cancellation, overall gain, and discriminator thresholds were all fine-tuned on a channel-by-channel basis for optimal performance.

Pulses with amplitudes below the lower threshold are considered noise or bremsstrahlung and are rejected. Pulses with amplitudes above the upper threshold are due to highly ionizing particles (or long path length trajectories of very energetic particles) and are rejected as unwanted background. The low threshold ensures efficient detection of electrons which backscatter out of a detector after depositing only part of their energy. The upper threshold ensures detection of valid events in the presence of noise or low-energy bremsstrahlung which add to the pulse height. For more energetic electrons, the lower threshold is set at the energy corresponding to a minimum ionizing particle traversing a minimal path through the detector (400 keV). This assures efficient detection of energetic electrons that pass through the detector with little scattering. The detector closest to the aperture is shielded from direct electron access by a tungsten cover that is physically a part of the internal aperture piece. In the original instrument, small energy deposits in this channel were interpreted as being due to bremsstrahlung and large deposits as being produced by penetrating protons or cosmic rays. Since the new detector array had 18 detector areas, the bremsstrahlung channel was deleted, and its telemetry slot was used by the seventeenth electron detector.

## Channel Energy Response

Table 1 provides a list of the energy boundaries, electronic thresholds, and geometric-energy factors (GEF) for each of the channels. These geometric-energy factors are based on the laboratory calibration data obtained from the MEA just prior to final delivery in January, 1990. The data were obtained using a collimated electron beam consisting of a $Sr^{90}$ source viewed through sets of collimators and a large bending magnet (90 deg) for energy selection. The energy response of each channel at 0-deg incident beam was matched to numerical calculations of the expected energy response for a 180-deg magnetic spectrometer with the collimator geometry of the combined release and radiation effects satellite (CRRES) instrument. This was necessary because the field in the magnet chamber was nonuniform (the result of a small chip of Indox V magnet material flaking off due to differential thermal contraction during a cold soak at − 60°C). Prior to the cold soak (and the fracture of the magnet from the yoke), the chamber magnetic field was about 850 G and quite uniform. After rebonding the magnet pole piece to the yoke, remagnetizing the unit (in a somewhat nonuniform field), disassembling the yoke to stabilize the magnet, and finally reassembling the unit, the field varied from about 700–850 G at various positions within the chamber. Thus, a detailed recalibration was required. The calibration data were obtained after final "buttoning-up" of the spectrometer with the flight detector array and used the flight DPU to obtain data simultaneously in all channels at all test energies.

## Calibration

The geometric-energy factors are calculated factors based on test data taken at intervals of 10–30 keV over the range 95–1739 keV and have an estimated accuracy of about 1%. The energy response is accurate to 1 or 2%, also, provided the energy of the input beam was accurate to within 1%. The input beam was calibrated with conversion electrons from a radioactive source at a number of energies. The ultimate limit on knowledge of the energy calibrations is due to the finite widths of the collimator apertures within the bending magnet, which translate into finite widths of energy spread in the electron beam (varying from about 10 keV at the lowest test energies to about 35 keV at the highest energies). The energy profile of the beam was roughly rectangular (sharp cutoffs in energy at both the low and high sides). Finally, the geometric-energy factor calculations assume ~ 100% efficiency in the detection process. This is known, by laboratory test, to be a reasonable assumption. The test involved measuring a uniform electron beam (from a radioactive source) at 90 deg incidence using a single silicon detector-electronics channel and comparing the count rate with the count rate measured by a very thin window (2.4 mg/cm$^2$ of mica) Geiger-Müller (GM)

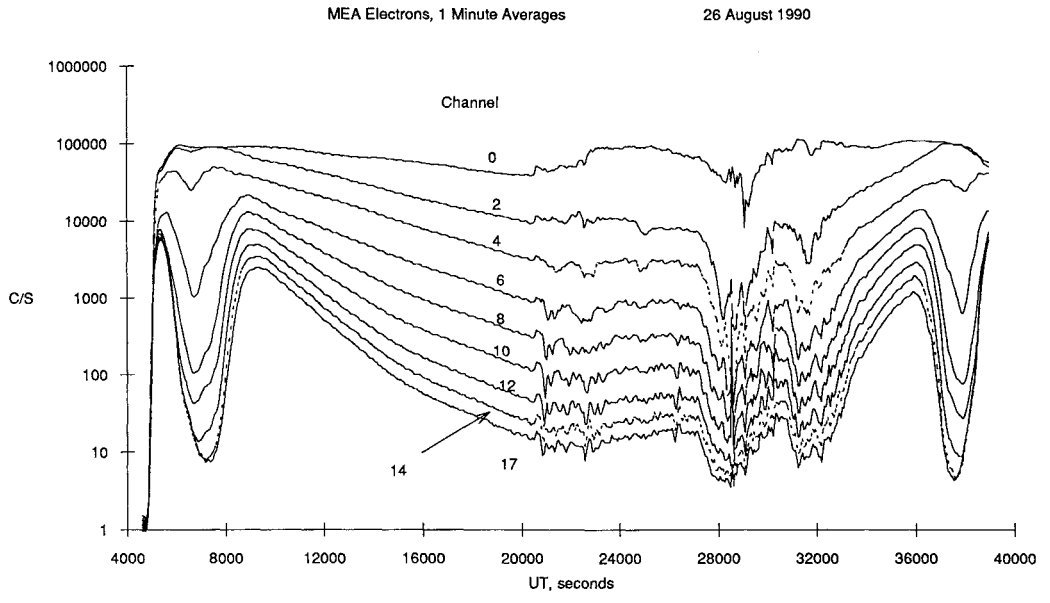


**Fig. 2 CRRES MEA electron data over one orbit.**

**Table 1 CRRES MEA channel response**

| Ch | $E_1$ | $E_{min}$ | $E_c$ | $E_{max}$ | $E_2$ | *GEF* | $B_{eff}$ | $Th_L$ | $Th_U$ | Angle |
|---|---|---|---|---|---|---|---|---|---|---|
| 0 | 78 | 110 | 153 | 188 | 240 | 5.88 | 860 | 38 | 250 | 8.24 |
| 1 | 136 | 174 | 214 | 257 | 310 | 5.68 | 818 | 73 | 350 | 6.37 |
| 2 | 190 | 230 | 271 | 314 | 365 | 5.16 | 765 | 115 | 400 | 5.19 |
| 3 | 255 | 297 | 340 | 384 | 435 | 4.84 | 740 | 160 | 500 | 4.38 |
| 4 | 330 | 374 | 418 | 462 | 513 | 4.59 | 727 | 200 | 600 | 3.78 |
| 5 | 421 | 465 | 510 | 553 | 608 | 4.19 | 710 | 275 | 750 | 3.24 |
| 6 | 512 | 558 | 604 | 649 | 701 | 3.89 | 713 | 330 | 900 | 2.90 |
| 7 | 598 | 646 | 693 | 738 | 790 | 3.58 | 710 | 380 | 1000 | 2.63 |
| 8 | 686 | 735 | 782 | 829 | 881 | 3.30 | 707 | 400 | 1100 | 2.40 |
| 9 | 778 | 828 | 876 | 923 | 975 | 3.08 | 707 | 400 | 1200 | 2.21 |
| 10 | 877 | 928 | 976 | 1024 | 1076 | 2.89 | 709 | 400 | 1300 | 2.05 |
| 11 | 989 | 1042 | 1090 | 1139 | 1191 | 2.66 | 706 | 400 | 1450 | 1.88 |
| 12 | 1078 | 1131 | 1178 | 1227 | 1278 | 2.49 | 702 | 400 | 1550 | 1.76 |
| 13 | 1185 | 1239 | 1287 | 1337 | 1389 | 2.37 | 707 | 400 | 1650 | 1.66 |
| 14 | 1268 | 1322 | 1370 | 1419 | 1470 | 2.23 | 700 | 400 | 1750 | 1.56 |
| 15 | 1368 | 1423 | 1470 | 1520 | 1570 | 2.14 | 702 | 400 | 1900 | 1.48 |
| 16 | —[a] | — | — | — | — | — | — | 200 | 2000 | — |
| 17 | 1478 | 1534 | 1582 | 1633 | 1684 | 2.03 | 706 | 400 | 2000 | 1.41 |

[a]Background.

**Table 2 CRRES MEA view angles**

| | Nominal, deg | Actual, deg |
|---|---|---|
| Normal to the spin plane | 4.92 | 11.58 |
| In the spin plane | 6.41 | 16.20 |

tube. Count rates were identical (within statistics) at all energies down to about 115 keV, at which point the GM tube was only 99% efficient compared to the silicon detector, and 97% at 90 keV. The test was terminated at 90 keV.

In Table 1, *GEF* and $B_{eff}$ are the geometric-energy factor and effective field strength, respectively. The $Th_{L,U}$ are the lower and upper electronic thresholds set on each channel pulse-height discriminator. $E_1$ and $E_2$ are the lowest and highest energy electrons that can reach the detector without being scattered into it. $E_{min}$ and $E_{max}$ are the nominal lower and upper energies of the channel. More than 90% of the total response of the channel is between these two energies. $E_c$ is the center of the response in that 50% of the *GEF* is above and 50% below this value. The peak response of the channel is very close to this value (within 1 or 2%). The nominal cutoff energies are determined in the following manner: The energy at which the peak response occurs is determined. Initial high- and low-energy cutoff values (10% of the peak value) are determined. A linear least-squares fit is made separately to the response between $E_{min,10\%}$ and $E_c$ and between $E_c$ and $E_{max,10\%}$. The zero intercepts of these fits are then listed as the $E_{min}$ and $E_{max}$. The *GEF* is the integral under the original curve. The energies are given in kiloelectron volts and the GEF are in units of cm$^2$-s-ster-keV. Thus, the counts/s must be divided by this number to transform to flux. Note that the counts in the data stream are counts per 0.512 s and are telemetered in a compressed floating-point format.

## Channel Angular Response

The MEA is mounted on one wall of CRRES compartment 4 with the horizontal plane parallel to the spacecraft spin axis and the normal to the aperture perpendicular to the spin axis. It is canted 10 deg away from the wall to ensure that a wire boom extending parallel to the wall is outside of its field of view. In the list below, and in Table 1, all angles are half-angles—the total field of view is ± these angles. The collimator limiting angles are given in Table 2. The actual collimator angles are larger than the nominal angles due to the finite length of the collimator. The actual channel limiting angles in the spin plane (due to detector location in chamber) are listed in the last column of Table 1.

## On-Orbit Performance

The MEA has been producing excellent data since its initial turn-on during Orbit 5 on July 27, 1990. The large geometric factor provides excellent statistics, even at low levels of flux. This does have its drawback, however. To provide noise immunity in the channels after significant detector degradation occurs due to radiation damage, relatively long pulse shaping times were used. The result is a limiting count rate of about 120,000 counts/s. Above 60,000 counts/s the count-rate curve becomes nonlinear (i.e., some counts are missed). In flux extremes, the lowest two channels have exhibited saturation in count rate. These nonlinearities can be corrected in the data analysis. The narrow acceptance angle in the spin plane provides very good pitch-angle resolution, especially at high energy. The full field of view, coupled with the angular scan of 6 deg which occurs during the 0.512-s data accumulation period, results in a total acceptance angle within a single data sample of about 8–18 deg, depending on channel. The true pitch angle distribution of the particles can be established to about 0.5 deg through a deconvolution procedure which is limited by the accuracy of the onboard magnetometer data

and by the statics of the counts in the samples. Figure 2 shows typical on-orbit performance. The data were obtained on August 26, 1990 and consist of 60-s averages of raw count rates in alternate channels, beginning with the lowest energy channel (Ch 0). The plot starts at perigee below the particle trapping region of the magnetosphere, goes up through the inner zone, through the slot, and out into the outer zone. Just after 20,000 s UT, a minor magnetic storm occurs. The effect on the energetic electrons is quite evident. The vehicle then goes back through the slot and into the inner zone. At that point the vehicle was put into a LASSII mode and the MEA data stopped. The data have not been corrected for proton contamination in the inner zone.

### Acknowledgments

Construction and integration of this instrument was funded under Air Force Space Systems Division Contract F0471-88-089. The authors thank G. Boyd, D. Chennette, J. Cowder, C. Holmes, S. Imamoto, N. Katz, R. Koga, and P. Lew, all of whom contributed significantly to the successful on-orbit operation of this instrument.

### References

[1]Siegbahn, K. (ed.), *Beta- and Gamma-Ray Spectroscopy,* Interscience, New York, 1955, pp. 52–99.

[2]Koga, R., Imamoto, S. S., Katz, N., and Pinkerton, S. D., "Data Processing Units for Eight Magnetospheric Particle and Field Sensors," *Journal of Spacecraft and Rockets,* Vol. 29, No. 4, 1992, pp. 574–579.

## Proton Switches

J. B. Blake* and S. S. Imamoto†
*The Aerospace Corporation, Los Angeles, California 90009*

THE proton switches (PS) are two omnidirection detectors, sensitive to protons (and heavier ions). The name proton switch has an historical origin. They were used in a mission 20 years ago (OV1-20PM) for turning on a high-power payload when energetic protons were present, and turning it off when the proton flux dropped below a preset value. In its first incarnation SPACERAD was to have been a simple, duty-cycled payload.

The PS detectors are Li-drifted silicon with a cubical shape, 3 mm on an edge. A uniform hemispherical shield is placed over the upper $2\pi$ solid angle; the rear $2\pi$ solid angle is shielded far more massively. The configuration is shown in Fig. 1. The detectors are connected to the usual preamplifier, amplifier, and discriminator electronic systems. The discriminator levels are chosen to be several times the energy which an electron can deposit in the detector. As a result, only protons and heavier ions are detected, and background caused by electron pileup is nil. The energy threshold is determined by the thickness of the hemispherical shield and, to a much smaller degree, by the discriminator thresholds. The hemispherical shields for the SPACERAD sensors were chosen to be 20 MeV and 50 MeV (for protons).

A zeroth-order estimate of the geometric factor is computed in the following way. The efficiency $\epsilon(E,E_B)$ is calculated from proton range-energy tables and geometric considerations, i.e., the path-length distribution converted to energy deposit for a given discriminator level $E_B$. The geometric factor is defined by the following expression:

$$\bar{\epsilon}\int_{E_l}^{E_u} e^{-E/E_0} = \int_{E_l}^{E_u} \epsilon(E,E_B)e^{-E/E_0}$$

where the subscripts $l$ and $u$ refer to the lower and upper limits of the energy channel. The lower level $E_l$ is fixed by the shield and $E_B$ is set by the electronic threshold. Therefore the integration given above is carried out for values of $E_0$ of geophysical interest and for a series of values for $E_u$. The value of $E_u$ is selected such that the geometric factor is independent of the spectral index. Similar calculations have been carried out for power-law spectra; the results are much the same. Table 1 gives the geometric factor for the four PS channels for exponential spectra.

It is important to note the assumption that goes into the calculations of geometric factor and energy passband—that the spectral shape is either exponential or power-law and fixed over the entire energy range of integration. In the inner zone, it is conventional wisdom that the proton spectra are exponentials over a large energy range, cf. AP-8. In the case of solar-flare spectra, this assumption usually is not a good one. *The geometric factors and passbands are gross approximations only, and must be used with care.*

A conversion of count rate to proton flux can be made readily by using the large arrays of calculated values for $\epsilon(E,E_B)$; this must be done for quantitative work. (The calculated efficiencies as a function of energy are available from the authors.) However, the major purpose for including these two sensors in the SPACERAD payload was to provide guidance in the analysis of the data from the more sophisticated sensors—is there a penetrating proton background, about how large is it, and what roughly is the spectral shape? These purposes are well served by the information in Table 1.

It was noted above that these sensors have no electron sensitivity. However, they do show a very low count rate due to galactic cosmic rays. Since there are very few cosmic rays in the passbands of the proton switches, the major causes of these background counts are nuclear interactions in the detector itself and neutron-induced reactions in the detector where the neutrons are secondaries generated in the spacecraft. This low cosmic-ray background varies over the combined release and radiation effects satellite (CRRES) orbit because of the variations in geomagnetic cutoff.

Figure 2 is a line plot of the output of the two sensors for a partial orbit including the inner zone where the trapped energetic protons are found. The upper trace is for the sensor with the 20-MeV shield (lower energy threshold); the lower one for the 50-MeV shield (lower energy threshold). This figure clearly shows the sensor characteristics described above. Note the immunity to background counts from electrons; away from the broad peaks due to the inner zone protons only the very low residual galactic cosmic-ray background can be seen. It also is easy to see that near perigee (34,999–35,000 s), where many of the galactic cosmic rays are excluded by the Earth's magnetic field, the background rate indeed is significantly reduced compared to the background count rate seen elsewhere.

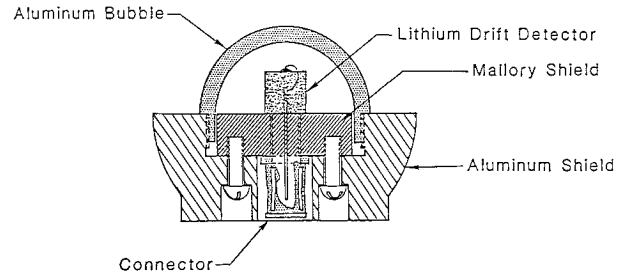


**Fig. 1 A cross section of a proton switch sensor is shown with the key components labeled.**

Received June 6, 1991; revision received Aug. 9, 1991; accepted for publication Aug. 9, 1991. 

*Director, Space Particles and Fields Department, Space and Environmental Technology Center, P.O. Box 92957.

†Research Engineer, Space Particles and Fields Department, Space and Environmental Technology Center, P.O. Box 92957.